



Article

Novel Two-Dimensional Layered MoSi_2Z_4 ($\text{Z} = \text{P}, \text{As}$): New Promising Optoelectronic Materials

Hui Yao^{1,2}, Chao Zhang³, Qiang Wang¹, Jianwei Li¹, Yunjin Yu^{1,*}, Fuming Xu¹, Bin Wang^{1,*} 
and Yadong Wei¹ 

¹ College of Physics and Optoelectronic Engineering, Shenzhen University, Shenzhen 518060, China; yaohui@szu.edu.cn (H.Y.); qiangwang@szu.edu.cn (Q.W.); jianweili@szu.edu.cn (J.L.); xufuming@szu.edu.cn (F.X.); ywei@szu.edu.cn (Y.W.)

² Laboratory of Optoelectronic Devices and Systems of Ministry of Education and Guangdong Province, College of Physics and Optoelectronic Engineering, Shenzhen University, Shenzhen 518060, China

³ Beijing Computational Science Research Center, Beijing 100193, China; chaozhang@csrc.ac.cn

* Correspondence: yuyunjin@szu.edu.cn (Y.Y.); binwang@szu.edu.cn (B.W.)

Abstract: Very recently, two new two-dimensional (2D) layered semi-conducting materials MoSi_2N_4 and WSi_2N_4 were successfully synthesized in experiments, and a large family of these two 2D materials, namely MA_2Z_4 , was also predicted theoretically (Science, 369, 670 (2020)). Motivated by this exciting family, in this work, we systematically investigate the mechanical, electronic and optical properties of monolayer and bilayer MoSi_2P_4 and MoSi_2As_4 by using the first-principles calculation method. Numerical results indicate that both monolayer and bilayer MoSi_2Z_4 ($\text{Z} = \text{P}, \text{As}$) present good structural stability, isotropic mechanical parameters, moderate bandgap, favorable carrier mobilities, remarkable optical absorption, superior photon responsivity and external quantum efficiency. Especially, due to the wave-functions of band edges dominated by d orbital of the middle-layer Mo atoms are screened effectively, the bandgap and optical absorption hardly depend on the number of layers, providing an added convenience in the experimental fabrication of few-layer MoSi_2Z_4 -based electronic and optoelectronic devices. We also build a monolayer MoSi_2Z_4 -based 2D optoelectronic device, and quantitatively evaluate the photocurrent as a function of energy and polarization angle of the incident light. Our investigation verifies the excellent performance of a few-layer MoSi_2Z_4 and expands their potential application in nanoscale electronic and optoelectronic devices.

Keywords: DFT; remarkable optical absorption; superior external quantum efficiency; optoelectronic devices



Citation: Yao, H.; Zhang, C.; Wang, Q.; Li, J.; Yu, Y.; Xu, F.; Wang, B.; Wei, Y. Novel Two-Dimensional Layered MoSi_2Z_4 ($\text{Z} = \text{P}, \text{As}$): New Promising Optoelectronic Materials. *Nanomaterials* **2021**, *11*, 559. <https://doi.org/10.3390/nano11030559>

Academic Editor: Jung-Ho Yun, Jeonghun Kim and Francisco Javier García Ruiz

Received: 3 February 2021

Accepted: 20 February 2021

Published: 24 February 2021

Publisher's Note: MDPI stays neutral with regard to jurisdictional claims in published maps and institutional affiliations.



Copyright: © 2021 by the authors. Licensee MDPI, Basel, Switzerland. This article is an open access article distributed under the terms and conditions of the Creative Commons Attribution (CC BY) license (<https://creativecommons.org/licenses/by/4.0/>).

1. Introduction

Two-dimensional (2D) materials have attracted extensive attention due to their distinctive physical and material properties and the potential application on account of monolayer limit [1–9]. As a typical representative, graphene has been widely expected to be a proper material for the preparation of a new generation of nanoelectronic devices due to remarkable high carrier mobility, but its zero bandgap reminds us that it may not be an effective solution [1,10,11]. Transition metal dichalcogenides (TMDCs) possess tunable bandgap, but its comparatively low carrier mobilities is a not neglectable obstacle for practical applications [3,12–14]. For example, the carrier mobility of MoS_2 is roughly $72 \text{ cm}^2\text{V}^{-1}\text{s}^{-1}$ for electron and $200 \text{ cm}^2\text{V}^{-1}\text{s}^{-1}$ for hole, which are roughly four to six orders of magnitude smaller than graphene and even much lower than those of low-doped Si ($1350 \text{ cm}^2\text{V}^{-1}\text{s}^{-1}$ for electron and $480 \text{ cm}^2\text{V}^{-1}\text{s}^{-1}$ for hole). Beyond TMDCs, a large 2D family of transition metal carbides and carbonitrides, called MXenes, has been discovered in recent years [15–17]. MXenes are produced by the etching out of the A layers from MAX phases of $\text{M}_{n+1}\text{AX}_n$, where M is a transition metal, A is mainly a group IIIA or IVA element, and

X is C or N with $n = 1, 2, 3$. So far, more than 60 different pure MXenes have been explored. Their electronic properties, such as band-gap and magnetism, can be tuned by changing the MXene elemental composition and the surface terminations.

Very recently, a new kind of hexagonal 2D MXene, MoSi_2N_4 and WSi_2N_4 , was successfully synthesized by chemical vapor deposition method with large size up to $15 \text{ mm} \times 15 \text{ mm}$ [18]. They show good environmental stability, and even have no structural deformation within six months. Monolayer MoSi_2N_4 is septuple-atomic-layer structure of N-Si-N-Mo-N-Si-N, which can be view as a MoN_2 layer sandwiched by two SiN layers. It exhibits indirect bandgap semiconducting behavior with band-gap roughly equal to 1.94 eV. The elastic modulus is four times that of monolayer MoS_2 , and electron/hole mobility is also roughly four-to-six times larger than that of monolayer MoS_2 . In addition, a large family of MA_2Z_4 is predicted by first-principles calculation, where M represents the elements of IVB, VB, or VIB groups, A represents Si or Ge, and Z represents the elements of VA group. The nanosheets in this family are expected to have wide tunable bandgap and magnetic properties, meaning potential application in electronics, optoelectronics and spintronics.

Motivated by the exciting properties of MoSi_2N_4 and WSi_2N_4 , some theoretical works have been carried out to further explore the mechanical and physical properties of their family by using the first-principles calculation method [19,20]. The lattice thermal conductivity, piezoelectric and flexoelectric response, and photocatalytic and electronic feature of monolayer MA_2Z_4 (M = Cr, Mo, W; A = Si, Ge; Z = N, P) were systematically calculated. They show diverse electronic properties from antiferromagnetic metal to half metal and semiconductor with band gaps ranging from 0.31 to 2.57 eV. Monolayer MoSi_2N_4 and WSi_2N_4 were predicted to show outstandingly high lattice thermal conductivity of 440 and 500 W/mK, respectively [19]. The piezoelectricity property was calculated for six different configurations of MSi_2N_4 (M = Mo, W) which are built through translation, mirror and rotation operations. The maximum piezoelectric strain and stress coefficients is 3.53 pm/V and $13.95 \times 10^{-10} \text{ C/m}$ for MoSi_2N_4 , and 2.91 pm/V and $12.17 \times 10^{-10} \text{ C/m}$ for WSi_2N_4 , respectively, which are much larger than those of 2D TMD, metal oxides, III-V semiconductor and Janus TMD [20]. By tuning biaxial in-plane strain to monolayer VSi_2P_4 , a continuous phase transition can be occurred from a ferromagnetic metal to a spin-gapless semiconductor to a ferromagnetic semiconductor to spin-gapless semiconductor to a ferromagnetic half-metal. At the ferromagnetic semiconductor phase, ferromagnetism and piezoelectricity can exist together due to broken inversion symmetry [21]. The van der Waals hetero-structures composed of MoSi_2N_4 contacted by graphene and NbS_2 monolayers were predicted to exhibit ultra-low Schottky barrier height, which can be modulated via the interlayer distance or external electric field [22]. Due to the intrinsic inversion symmetry breaking and strong spin-orbital coupling, remarkable spin-valley coupling in the inequivalent valleys at K and K' points can be found for MoSi_2X_4 (X = N, P, As). It induces spin-valley coupled optical selection properties, which can be tuned by in-plane strain [23]. Beyond traditional two-level valleys, monolayer MoSi_2N_4 shows multiple folded valleys, implying an additional intrinsic degree of freedom. The valley-contrasting properties in monolayer MoSi_2N_4 were discussed by using a three-band low-power Hamiltonian, where each valley and energy band can be selectively controlled [24].

In this paper, we systematically investigate the structural, electronic, optoelectronic and quantum transport properties of monolayer and bilayer MoSi_2Z_4 (Z = P, As). All these 2D materials possess stable configuration, moderate direct band-gap, high and anisotropic carrier mobilities, large optical absorption coefficient, superior photon responsivity and external quantum efficiency in the visible light region. An optoelectronic device based on monolayer MoSi_2Z_4 is also built to model the adjustable photocurrent. Our investigation further expands the application prospect of few-layer MoSi_2Z_4 in nanoelectronics and optoelectronics.

The rest of this paper is organized as follows. In Section 2, the computational methods are briefly introduced. In Section 3, the numerical results of the structural, electronic

and optoelectronic properties are presented. In addition, the photocurrent of monolayer MoSi_2Z_4 -based nanodevice is also calculated. In Section 4, a brief summary is presented.

2. Numerical Methods

A first-principles calculation is performed by using the Vienna *ab initio* simulation package [25,26] based on the density functional theory (DFT). Both the generalized gradient approximation with a PBE form [27] and the Heyd-Scuseria-Ernzerhof (HSE06) [28] hybrid functional is adopted to calculate the band structures and optical-electronic properties. The energy cutoff and reciprocal k-points are chosen as 500 eV and $16 \times 16 \times 1$ in structure relaxation and electronic calculation. A vacuum space of 20 Å perpendicular to the 2D plane is applied to separate the periodic images. The weak vdW interaction between adjacent layers is described by the DFT-D2 functional with Grimme correction [29]. The convergence criteria of force and energy are set to 0.01 eV/Å and 10^{-5} eV. To examine the stability of all the structures, PHONOPY code is used to calculate the phonon dispersion curves [30], and *ab initio* molecular dynamics (AIMD) simulation [31] is carried out to examine the total energy evolution at high temperature. To calculate the photocurrent of 2D layered MoSi_2Z_4 based nanodevice, Nanodcal software is evaluated which is developed based on the combination of DFT and non-equilibrium Green's function (NEGF-DFT) [32]. In the calculation, norm-conserving pseudopotential, double-zeta polarization basis set and exchange-correlation functional at PBE level are employed.

3. Results and Discussion

3.1. Structural and Mechanical Properties of Few-Layer MoSi_2Z_4 ($Z = \text{P, As}$)

Figure 1 shows the optimized schematic structures of monolayer (a) and bilayer (b–d) MoSi_2Z_4 from top view and side view, where $Z = \text{P, As}$. Monolayer MoSi_2Z_4 is constructed from septuple atomic layers of $Z\text{-Si-Z-Mo-Z-Si-Z}$, which can be viewed as a MoZ_2 layer sandwiched by two SiZ layers. It presents A–B stacked hexagonal lattice from the top view, and its primitive cell includes one Mo atom, two Si atoms and four Z atoms as labeled by the parallelogram in Figure 1a. The lattice parameters $a = b = 3.470$ Å and 3.620 Å for $Z = \text{P}$ and As , respectively, which are well coincident with those predicted in previous work [18]. Figure 1b–d present three most likely stacking patterns of bilayer MoSi_2Z_4 , namely AA, AB and AC, where the Si atoms in the lower layer are aligned with the Si, Z, and Mo atoms in the upper layer, respectively. The relaxed lattice parameters a and interlayer distances d are listed in Table 1 for each stacking pattern and two kinds of Z atoms. We find that the interlayer distance of AB stacking is the smallest compared to the other two stacking patterns for both MoSi_2P_4 and MoSi_2As_4 .

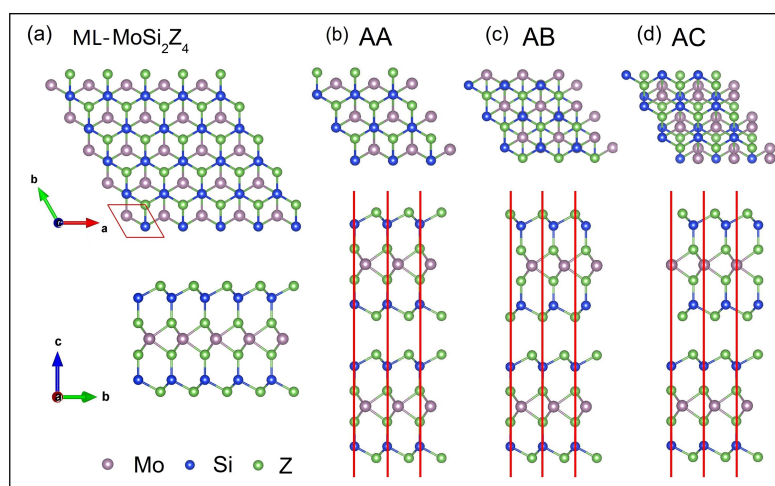


Figure 1. (a) Schematic structure of monolayer MoSi_2Z_4 ($Z = \text{P, As}$) from top view and side view. The parallelogram indicates its primitive cell. (b) AA, (c) AB, (d) AC stacking patterns of bilayer MoSi_2Z_4 .

Table 1. Lattice constants a , interlayer distance d , cohesive energy E_c , binding energy E_b and band gap of few-layer MoSi_2Z_4 ($Z = \text{P, As}$).

System Patterns	Monolayer	Bilayer MoSi_2P_4			Monolayer	Bilayer MoSi_2As_4		
	MoSi_2P_4	AA	AB	AC	MoSi_2As_4	AA	AB	AC
$a(\text{\AA})$	3.470	3.449	3.450	3.450	3.620	3.581	3.583	3.583
$d(\text{\AA})$	—	3.850	3.075	3.081	—	3.825	3.108	3.112
$E_c(\text{eV})$	−6.089	—	—	—	−5.475	—	—	—
$E_b(\text{eV})$	—	−3.536	−3.614	−3.613	—	−4.272	−4.385	−4.384
Bandgap(eV)	1.015	0.994	1.019	1.021	0.891	0.888	0.894	0.894

Firstly, we check the stability of monolayer and bilayer MoSi_2Z_4 before further studying their physical properties. For monolayer MoSi_2Z_4 , the cohesive energy is calculated by

$$E_c = (E_{\text{Mo}} + 2E_{\text{Si}} + 4E_{\text{Z}} - E_{\text{MoSi}_2\text{Z}_4})/7, \quad (1)$$

where E_{Mo} , E_{Si} , E_{Z} and $E_{\text{MoSi}_2\text{Z}_4}$ are total energies of isolated Mo atom, Si atom, Z atom and a primitive cell of MoSi_2Z_4 . The calculated cohesive energies are 6.089 eV/atom for MoSi_2P_4 and 5.475 eV/atom for MoSi_2As_4 . They are smaller than that of graphene (7.46 eV/atom), while larger than those of MoS_2 (4.98 eV/atom) and phosphorene (3.30 eV/atom) [33–35] indicating proper stability. For bilayer MoSi_2Z_4 , the stability is generally measured by the binding energy defined as

$$E_b = E_{\text{BL}} - 2E_{\text{ML}}, \quad (2)$$

where E_{BL} and E_{ML} stand for total energies of bilayer and monolayer MoSi_2Z_4 , respectively. As listed in Table 1, the binding energies are negative for all the bilayer MoSi_2Z_4 , and the AB stacking has the smallest value indicating the most stable stacking pattern. Thus, we only focus on the AB stacking pattern for the bilayer MoSi_2Z_4 in the rest of this paper.

Next, the phonon dispersion spectrums of monolayer MoSi_2Z_4 are calculated to examine their dynamic stability. Figure 2a presents the phonon dispersion spectrum of monolayer MoSi_2P_4 . The low-frequency band near Γ point is roughly linear and there is no imaginary modes in the Brillouin zone, which indicates monolayer MoSi_2P_4 is dynamically stable. An AIMD simulation is performed at 300 K to further examine the thermal stability of the structure by employing a 4×4 supercell. As shown in Figure 2b, the total energy of monolayer MoSi_2P_4 oscillates slightly in the vicinity of -720 eV for a long time without decay. Neither bond-breaking nor geometry reconstruction appears in the structure at 10 fs indicating thermal stability of monolayer MoSi_2P_4 at room temperature. Similar phonon dispersion spectrums and total energy evaluations are also obtained for all the other monolayer and bilayer structures, as shown in Figure 3.

Finally, we examine the mechanical properties of all the structures under external force by calculating elastic constants C_{ij} . As listed in Table 2, the Born criteria $C_{11}C_{22} - C_{12}^2 > 0$ and $C_{66} > 0$ are both satisfied for the monolayer and bilayer MoSi_2Z_4 meaning their mechanical stability [36]. Based on $C_{i,j}$, Young's modulus $Y(\theta)$ and the Poisson's ratio $\nu(\theta)$ along the in-plane angle θ and the layer modulus γ are also calculated. $Y(\theta)$ indicates the reciprocal of the response of strain to stress along a specific direction along θ in the 2D plane. $\nu(\theta)$ is the ratio of the absolute value of transverse normal strain to axial normal strain. γ represents the resistance of the 2D surface to stretching, and thus is independent of θ . These physical quantities can be calculated by the following formulas [37]

$$Y(\theta) = \frac{C_{11}C_{22} - C_{12}^2}{C_{11} \sin^4 \theta + A \sin^2 \theta \cos^2 \theta + C_{22} \cos^4 \theta},$$

$$\nu(\theta) = \frac{C_{12} \sin^4 \theta - B \sin^2 \theta \cos^2 \theta + C_{12} \cos^4 \theta}{C_{11} \sin^4 \theta + A \sin^2 \theta \cos^2 \theta + C_{22} \cos^4 \theta},$$

$$\gamma = \frac{1}{4}(C_{11} + C_{22} + 2C_{12}),$$

in which $A = (C_{11}C_{22} - C_{12}^2)/C_{66} - 2C_{12}$ and $B = C_{11} + C_{22} - (C_{11}C_{22} - C_{12}^2)/C_{66}$. Figure 2c,d show the $Y(\theta)$ and $\nu(\theta)$ of monolayer MoSi_2Z_4 . $Y(\theta)$ is isotropic and $\nu(\theta)$ is roughly isotropic for both monolayers. $Y(\theta)$ of MoSi_2P_4 is larger than that of MoSi_2As_4 , while $\nu(\theta)$ of the former is smaller than that of the latter. This means monolayer MoSi_2As_4 is easier to deform under in plane external force than monolayer MoSi_2P_4 . It is reasonable because the As–Mo and As–Si bonds are longer and deformable than the P–Mo and P–Si bonds. Similarly, γ of MoSi_2P_4 is larger than that of MoSi_2As_4 . Y and γ of monolayer MoSi_2Z_4 are slightly smaller than that of monolayer graphene (340 N/m and 215.9 N/m) and BN (318 N/m and 177.0 N/m) [38], while comparable to those of SiC (179.7 N/m and 116.5 N/m) [38] and monolayer PC_3 (180.4 N/m and 102.1 N/m) [39] implying their similar mechanical response. In terms of bilayer MoSi_2Z_4 , both $Y(\theta)$ and γ are nearly two times as those of monolayer MoSi_2Z_4 (see Table 2 and Figure 3). Such behavior is physically reasonable and in good accordance with that of multilayer graphene [38] and PC_3 [39]. The calculated moduli indicate that few-layered MoSi_2Z_4 are stretchable and flexible as most of the other common 2D materials, indicating potential application in flexible electronic devices.

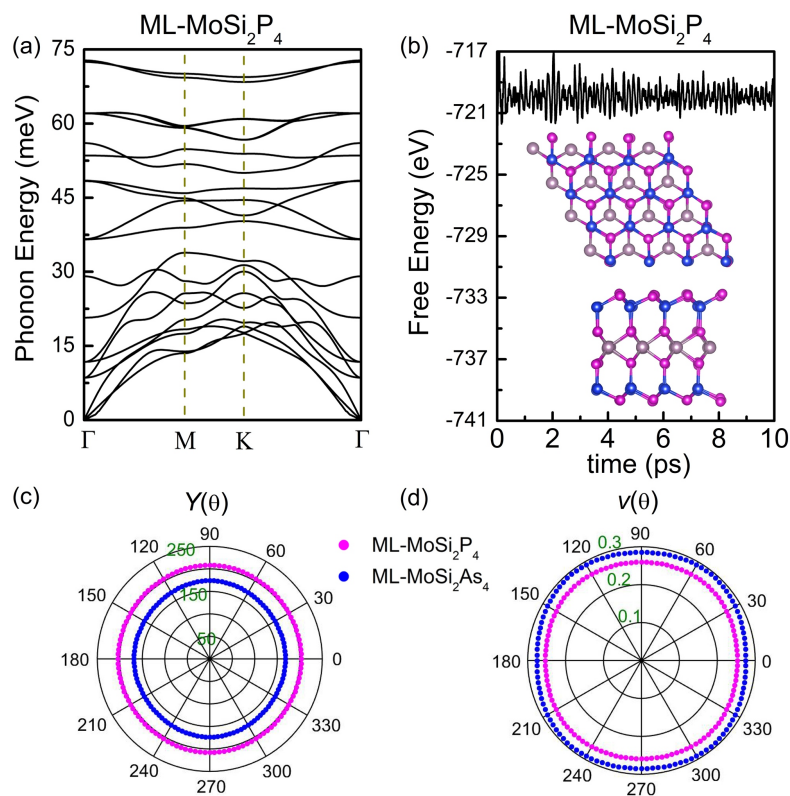


Figure 2. (a) Phonon dispersion curves and (b) total energy variation at 300 K of monolayer MoSi_2P_4 . Inset in (b) shows the top view and side view of a snapshot at 10 ps. (c) Young's modulus $Y(\theta)$ and (d) Poisson's ratio $\nu(\theta)$ of monolayer MoSi_2P_4 (purple curve) and MoSi_2As_4 (blue curve) along arbitrary in-plane directions.

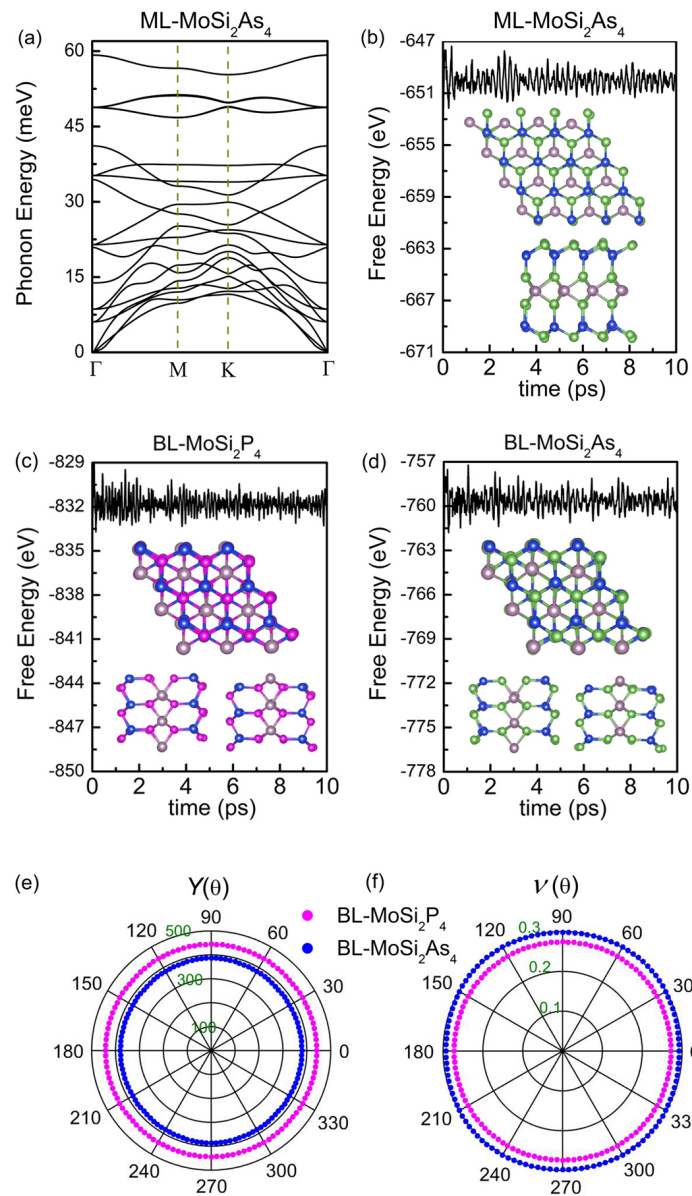


Figure 3. (a) Phonon band dispersion curves of the monolayer MoSi_2As_4 . Variations of total energy at 300 K as functions of time for (b) monolayer MoSi_2As_4 , (c) bilayer MoSi_2P_4 , (d) bilayer MoSi_2As_4 . (e) Young's modulus $Y(\theta)$ and (f) Poisson's ratio $\nu(\theta)$ of bilayer MoSi_2P_4 (purple curve) and MoSi_2As_4 (blue curve) along arbitrary in-plane directions.

Table 2. The calculated elastic constants C_{ij} , Young's modulus Y and Poisson's ratio ν along the x ($\theta = 0$) and y ($\theta = \pi/2$) directions, layer modulus γ for monolayer (ML-) and bilayer (BL-) MoSi_2Z_4 ($Z = \text{P, As}$).

Type	$C_{11}(\text{N/m})$	$C_{22}(\text{N/m})$	$C_{12}(\text{N/m})$	$C_{66}(\text{N/m})$	$Y_x(\text{N/m})$	$Y_y(\text{N/m})$	ν_x	ν_y	$\gamma(\text{N/m})$
ML- MoSi_2P_4	217.70	222.65	56.35	80.67	203.43	208.06	0.253	0.259	138.26
BL- MoSi_2P_4	476.59	479.76	130.42	173.09	441.14	444.07	0.272	0.274	304.30
ML- MoSi_2As_4	182.38	188.67	52.01	65.18	168.04	173.84	0.276	0.285	118.77
BL- MoSi_2As_4	415.86	423.43	124.00	145.93	379.54	386.45	0.293	0.298	271.82

3.2. Electronic Properties of Few-Layer MoSi_2Z_4

Figure 4a,b show the band structure and projected density of states (PDOS) of monolayer MoSi_2P_4 and MoSi_2As_4 based on PBE and HSE06 exchange-correlation functionals.

For each configuration, the band structure based on the PBE exchange-correlation functional is similar to that based on the HSE06 functional except the smaller bandgap. Both structures show a direct bandgap, and both conduction band minimum (CBM) and valence band maximum (VBM) locate at K point. This is different from monolayer MoSi_2N_4 , whose CBM sits K point while VBM locates at Γ point, presenting indirect band-gap semiconducting behavior (Ref. [18], also see Figure 5a). To get more insight into this difference, PDOS and charge distribution at VBM and CBM are plotted in Figure 5c,d. For monolayer MoSi_2P_4 and MoSi_2As_4 , both CBMs and VBMs are mainly originated from the d orbitals of Mo atoms which locate in the middle layer of the structures. While, for monolayer MoSi_2N_4 , VBM is dominated by both d orbital of Mo atoms and p orbital of Z atom (see Figure 5b). Due to the orbital hybridization, an obvious extension of VBM from the middle Mo atoms to beside the Z atoms occurs, which is much different from the charge distribution of VBMs in MoSi_2P_4 and MoSi_2As_4 . This is reasonable because the N–Mo bonds are shorter than the P–Mo and As–Mo bonds, and thus the orbital hybridization is more likely to happen in MoSi_2N_4 .

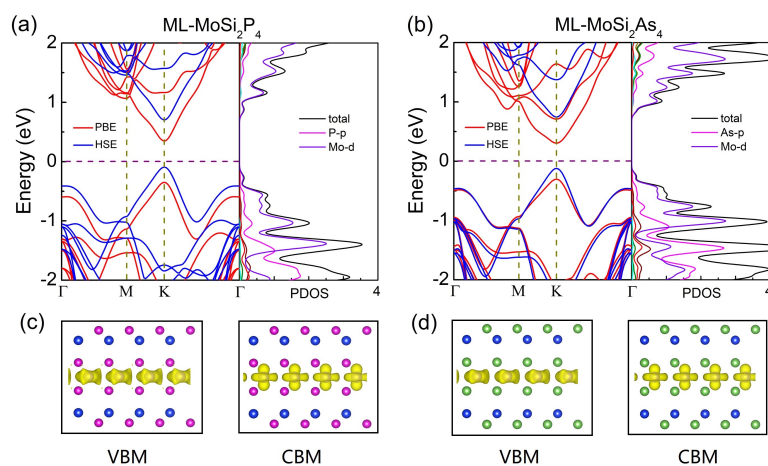


Figure 4. The electronic band structure and projected density of states (PDOS) of monolayer (a) MoSi_2P_4 and (b) MoSi_2As_4 . (c,d): Corresponding charge distribution at valence band maximum (VBM) and conduction band minimum (CBM) dominated by the d orbital of Mo atoms in the middle layer.

In terms of bilayer MoSi_2Z_4 , similar direct bandgap semiconducting behavior to monolayer MoSi_2Z_4 are obtained, where both CBM and VBM locate at K points (see Figure 5c,d). The bandgap of bilayer MoSi_2Z_4 changes very little in comparison to that of monolayer MoSi_2Z_4 (see Table 1). The independence of bandgap with the number of layers can be attributed to the orbital shield. Because the states at CBM and VBM are dominated by the d orbital of Mo atoms, they are effectively screened inside the monolayer MoSi_2Z_4 because the Mo atoms located in the middle layer of seven atomic layers. For bilayer MoSi_2Z_4 , the rather weak interlayer vdW interaction makes the Mo atoms at the up layer and those at the down layer have nothing to do with each other, and thus the band gap is very close to that of the monolayer. Similar layer number independent bandgap behavior has also been found in layered 2D KAgSe [40]. The layer number independent electronic properties provide enormous convenience and less difficulty in experimental fabrication of finite layer MoSi_2Z_4 -based electronic devices.

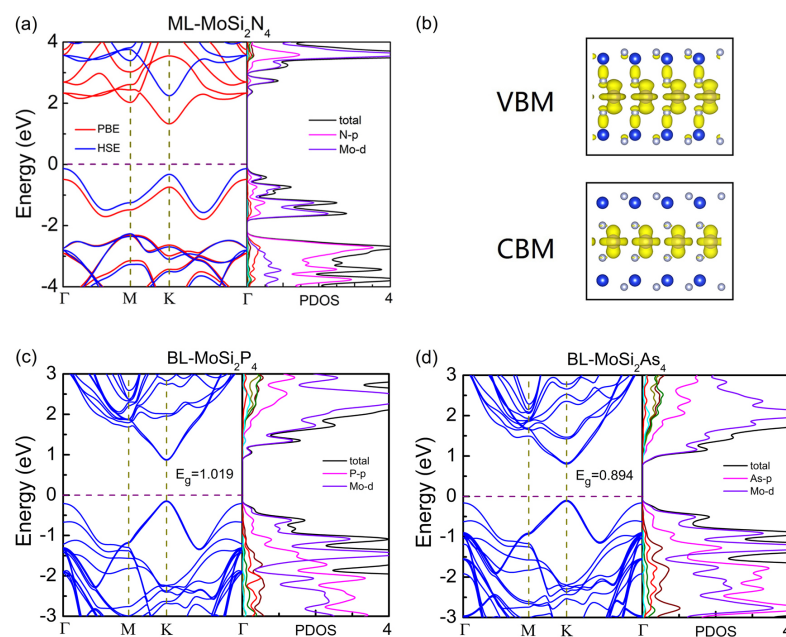


Figure 5. (a) The electronic band structure and PDOS of monolayer MoSi_2N_4 , (b) Corresponding charge distribution at VBM and CBM of monolayer MoSi_2N_4 . The electronic band structure and PDOS of bilayer (c) MoSi_2P_4 and (d) MoSi_2As_4 .

3.3. Carrier Mobilities of Few-Layer MoSi_2Z_4

Carrier mobility is an important factor to describe the transport ability of electronic and optoelectronic materials, which can be evaluated by using the deformation potential method as follows [41,42],

$$\mu = \frac{e\hbar C}{k_B T m^* m_d E_{DP}^2}, \quad (3)$$

where T is the temperature and equal to 300 K in this calculation; $m^* = \pm \hbar^2 (d^2 E_k / dk^2)$ is the effective mass of electrons and holes depending on the change of energy with wave vector k along different transport directions; m_d is the averaged effective mass defined as $m_d = \sqrt{m_x^* m_y^*}$; $C = (\partial^2 E / \partial^2 \epsilon) / S_0$ is the elastic modulus related to the change of total energy with strain along different directions; $E_{DP} = dE_{edge} / d\epsilon$ is the deformation potential constant given by the change rate of band edges with strain. The calculated carrier mobilities and corresponding parameters of layered MoSi_2Z_4 are summarized in Table 3.

Three pieces of information can be obtained from Table 3. Firstly, the carrier mobility of holes is roughly three to four times larger than that of electrons for both monolayer and bilayer MoSi_2Z_4 along with both x and y directions, which mainly attributes to the smaller deformation potential constant E_{DP} of holes. This difference of carrier mobilities can effectively facilitate the spatial separation of electrons and holes, which reduces the recombination probability of photo-excited carriers and suggests satisfactory performances for nanoscale electronic and optoelectronic devices. Secondly, the carrier mobilities of bilayer MoSi_2Z_4 are largely improved in contrast to those of monolayer MoSi_2Z_4 due to the roughly doubled elastic modulus C . Similar properties were also found for MXs [43]. Thirdly, the carrier mobilities of MoSi_2P_4 are slightly higher than that of MoSi_2As_4 for both monolayer and bilayer structures, which are also independent of carrier types and directions. Especially, these carrier mobilities are relatively high, which are much larger than those of MoS_2 ($200\text{--}500 \text{ cm}^2\text{V}^{-1}\text{s}^{-1}$) [44] and even comparable to those of black phosphorene [42] indicating potential application in 2D electronic devices.

Table 3. The effective mass m^* , elastic modulus C_{2D} , deformation potential constant E_{DP} , and carrier mobility μ along x and y directions for monolayer and bilayer MoSi_2Z_4 at 300 K.

System	Carrier Type	m^*/m_0	C_{2D} (Nm^{-1})	E_{DP} (eV)	μ ($\text{cm}^2\text{V}^{-1}\text{s}^{-1}$)
ML- MoSi_2P_4	e (x)	0.325	214.88	6.82	828.76
	e (y)	0.415	218.74	6.28	778.90
	h (x)	0.339	214.88	3.43	3171.83
	h (y)	0.430	218.74	3.65	2131.78
BL- MoSi_2P_4	e (x)	0.313	481.13	6.94	1919.84
	e (y)	0.403	484.88	6.40	1759.76
	h (x)	0.344	481.13	2.99	8652.25
	h (y)	0.435	481.88	3.55	4860.34
ML- MoSi_2As_4	e (x)	0.499	178.40	4.05	823.19
	e (y)	0.640	178.37	3.76	743.11
	h (x)	0.419	178.40	3.04	2093.38
	h (y)	0.524	178.37	3.16	1552.98
BL- MoSi_2As_4	e (x)	0.496	432.14	4.19	1855.52
	e (y)	0.659	432.12	3.88	1629.69
	h (x)	0.425	432.14	2.79	5905.10
	h (y)	0.528	432.12	2.77	4819.97

3.4. Optical Absorption Spectrums of Layered MoSi_2Z_4

Monolayer and bilayer MoSi_2Z_4 with direct band gaps about 0.85–1.0 eV exhibit potential application for visible–light solar harvesting/utilizing techniques or making narrow-gap semiconductor devices. Recent studies revealed that such narrow band gap materials are good candidates of infrared photodetectors, such as phosphorus carbides and black arsenic phosphorus [6,45,46]. Thus, we further investigate the optoelectronic performance of few-layer MoSi_2Z_4 by calculating the absorption coefficient as follows [47,48]

$$\alpha(\omega) = \sqrt{2}\omega \sqrt{\sqrt{\varepsilon_1^2(\omega) + \varepsilon_2^2(\omega)} - \varepsilon_1(\omega)}, \quad (4)$$

where c , ω , $\varepsilon_1(\omega)$ and $\varepsilon_2(\omega)$ stands for the light velocity, frequency of incident light, real part and imaginary part of the frequency-dependent dielectric function, respectively. $\varepsilon_1(\omega)$ and $\varepsilon_2(\omega)$ can be calculated by using the Kramers–Kronig relation and summing all the empty states in the Brillouin zone.

Figure 6 shows the optical absorption coefficients of monolayer and bilayer MoSi_2Z_4 based on PBE and HSE06 calculations, where the polarization direction of incident light is parallel to the 2D plane. All the few-layer MoSi_2Z_4 display very similar and remarkably high absorption coefficients ($\sim 10^5 \text{ cm}^{-1}$) in the visible-ultraviolet light region, which agrees well with their similar band gaps as shown in Figure 4. The large absorption is even comparable to that of graphene, phosphorene and MoS_2 [6]. The strong optical absorption and broad absorption ranges make layered MoSi_2Z_4 promising materials for photovoltaic solar cells and optoelectronic devices. Especially, the layer number independence to the bandgap and optical absorption makes the experimental fabrication more convenient of few-layer MoSi_2Z_4 -based 2D optoelectronic devices.

3.5. Photocurrent in Monolayer MoSi_2Z_4 Nanodevice

On account of the similar and excellent optical absorption performance of layered MoSi_2Z_4 , we build a monolayer MoSi_2Z_4 -based two-probe 2D optoelectronic device as shown in Figure 7 and evaluate its photoinduced current. To solve the quantum transport problem in this identical system, the device can be separated into three parts theoretically including a central scattering region and two semi-infinite electrodes. When the incident light energy in the scattering region is larger than the bandgap, the electrons at the valence band can be excited to the conduction band by absorbing photons. When a tiny external

bias is applied between the source and the drain, the excited electrons can be driven to produce photocurrent in the system. Note that the potential difference between the left and the right leads should be much smaller than the bandgap of the system to ensure that the detected current in the electrode is completely generated by the light but not bias. The photocurrent flowing into the left probe can be expressed in terms of the NEGF as follows [49–51],

$$J_L^{ph} = \frac{ie}{h} \int \text{Tr} \left[\Gamma_L \{ G^{<(ph)} + f_L(E)(G^{>(ph)} - G^{<(ph)}) \} \right] dE, \quad (5)$$

where f_L , Γ_L and $G^{</>(ph)}$ denotes the Fermi distribution function, line-width function and greater/lesser Green's function of the two-probe system including electron-photon interaction, respectively.

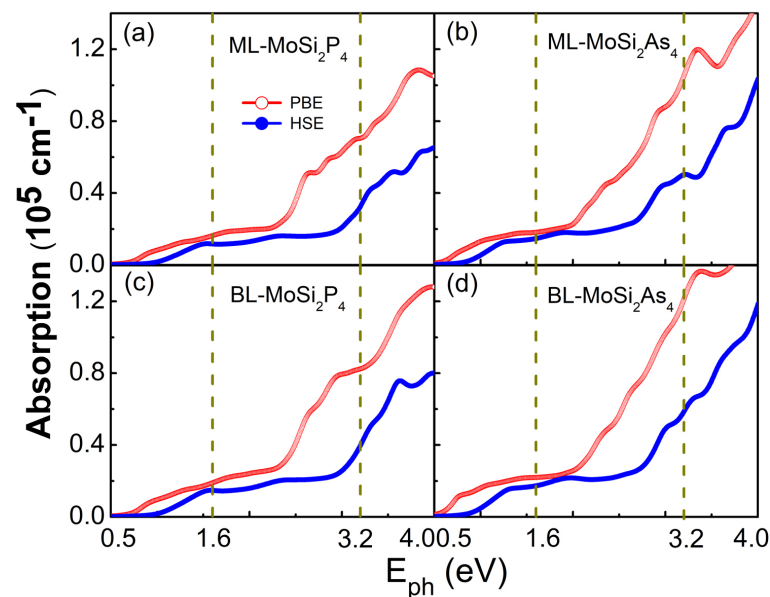


Figure 6. Optical absorption coefficients versus the energy of incident light for 2D (a) monolayer MoSi_2P_4 , (b) monolayer MoSi_2As_4 , (c) bilayer MoSi_2P_4 and (d) bilayer MoSi_2As_4 based on PBE and HSE06 functionals. For each panel, the polarization vector of incident light is set parallel to the plane, and the two vertical dashed lines indicate the region of visible light.

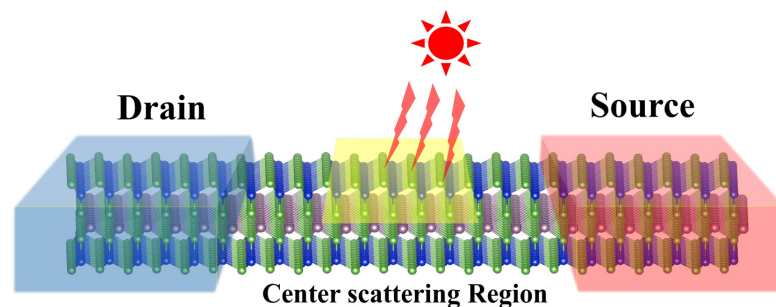


Figure 7. Schematic structure of monolayer MoSi_2Z_4 -based 2D optoelectronic device. The yellow zone in the center scattering region stands for the lighting area. The left blue region and right red region represent the drain and source, respectively.

In this calculation, the incident light is perpendicular to the 2D plane, and the angle between polarization direction and transport direction is labeled as θ . Figure 8a,c show the photocurrent versus energy of the linearly polarized light with power density equal to $10^3 \mu\text{W}/\text{mm}^2$ and θ equal to 0° and 90° . When energy is smaller than 0.5 eV, photocurrent

is equal to zero for both MoSi_2P_4 and MoSi_2As_4 because the energy is smaller than their band gaps. With further increase of energy, photocurrent appears and oscillates with the energy for both $\theta = 0^\circ$ and 90° depending on the detailed behavior of band structures. Photocurrent reaches local maximum in the visible region at $\theta = 0^\circ$, and in the ultraviolet region at $\theta = 90^\circ$. To further explore the influence of incident polarization angle θ , photocurrent as a function of θ under different photon energy in the visible light region are evaluated as shown in Figure 6b,d. For both MoSi_2P_4 and MoSi_2As_4 , the photocurrent is roughly symmetrical with respect to $\theta = 90^\circ$, and reaches maximums at $\theta = 0^\circ$ and $\theta = 180^\circ$. Similar symmetrical distribution of photocurrent with polarization angle was also reported for monolayer KAgSe -based 2D optoelectronic device [40].

The responsivity R_{ph} and external quantum efficiency τ_{eqe} are generally used to measure the photovoltaic performances, which are defined as

$$R_{ph} = \frac{J_L^{ph}}{eF_{ph}} \quad (6)$$

and

$$\tau_{eqe} = R_{ph} \frac{hc}{e\lambda}, \quad (7)$$

in which the photon flux F_{ph} stands for the number of incident photons in unit area and unit time. R_{ph} of monolayer MoSi_2P_4 and MoSi_2As_4 in the visible light region are 0.060 AW^{-1} and 0.046 AW^{-1} , respectively, which are the same order as those of MoS_2 (0.016 AW^{-1}) and monolayer chalcogenides (0.035 AW^{-1} for GeS and 0.075 AW^{-1} for SnS), while two orders higher than that of graphene ($5 \times 10^{-4} \text{ AW}^{-1}$) [52]. τ_{eqe} of monolayer MoSi_2P_4 and MoSi_2As_4 in the visible light region can reach 18.60% and 13.33%, respectively, which are comparable to those of KAgSe (17.92%) [40] and monolayer chalcogenides (10.27% for GeS and 22.01% for SnS) [53]. In addition, R_{ph} and τ_{eqe} of monolayer MoSi_2Z_4 are greatly increased within the whole light region, ie, 0.143 AW^{-1} and 64.26% for MoSi_2P_4 , 0.098 AW^{-1} and 41.16% for MoSi_2As_4 . Here, it is worth mentioning that the above values of photon responsivity R_{ph} and external quantum efficiency τ_{eqe} are all calculated theoretically based on the computational models. It is hoping that there will be more experimental results to support in the future. Once again, these ideal performances of MoSi_2Z_4 suggest their powerful potential application in optoelectronic and photovoltaic devices.

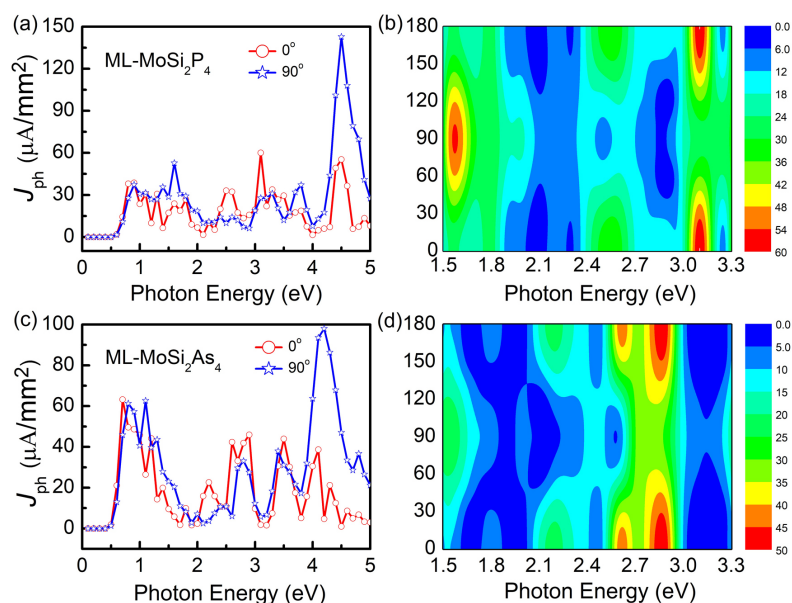


Figure 8. Photocurrent as a function of photon energy with polarization angle θ of the incident light equal to 0° and 90° for monolayer (a) MoSi_2P_4 and (c) MoSi_2As_4 nanodevice. (c,d) show the photocurrent versus photon energy and θ for monolayer (b) MoSi_2P_4 and (d) MoSi_2As_4 nanodevice.

4. Conclusions

Recently synthesized 2D semiconductors MoSi_2N_4 and WSi_2N_4 exhibit prominent material and physical properties, including remarkable stability, high strength and large carrier mobility, which also inspires increasing theoretical researches to further explore the physical properties of their family MA_2Z_4 . First principle calculations indicate that MA_2Z_4 materials possess wide tunable band gaps, magnetic properties and valley-contrasting properties, indicating potential applications in electronics, optoelectronics, spintronics and valleytronics. In this case, we investigated the electronic and photoelectrical properties of monolayer and bilayer 2D MoSi_2Z_4 ($Z = \text{P, As}$) by using the first-principles calculation method. Firstly, the structural, dynamic, thermal and mechanical stabilities of the few-layer MoSi_2Z_4 were numerically verified. Secondly, both monolayer and bilayer MoSi_2Z_4 show direct bandgap semiconducting behavior, which is different from MoSi_2N_4 with indirect bandgap. Moreover, the band gaps of layered MoSi_2Z_4 are roughly independent of the number of layers due to effective screening to the atomic orbital of Mo atoms. Thirdly, monolayer and bilayer MoSi_2Z_4 show high carrier mobilities and remarkable optical absorption coefficients. Monolayer MoSi_2Z_4 -based optoelectronic device displays large photon responsivity and external quantum efficiency. All these appealing properties make MoSi_2Z_4 promising candidates for application in electronic and optoelectronic devices.

Author Contributions: Conceptualization, H.Y. and B.W.; methodology, C.Z. and Q.W.; software, H.Y., J.L., F.X. and Y.W.; formal analysis, H.Y., B.W. and Y.Y.; investigation, H.Y. and C.Z.; writing-original draft preparation, H.Y.; writing-review and editing, B.W. All authors have read and agreed to the published version of the manuscript.

Funding: This work was financially supported by grants from the National Natural Science Foundation of China (NSFC) (Grant No. 11774238), Shenzhen Natural Science Foundations (Grant No. JCYJ20190808150409413, JCYJ20190808115415679 and JCYJ20190808152801642) and the Natural Science Foundation of Guangdong Province (GDNSF) (Grant No. 2020A1515011418).

Institutional Review Board Statement: Not applicable.

Informed Consent Statement: Not applicable.

Data Availability Statement: The data presented in this study are available on request from the corresponding author.

Conflicts of Interest: There are no conflicts of interest to declare.

References

1. Novoselov, K.S.; Geim, A.K.; Morozov, S.V.; Jiang, D.; Zhang, Y.; Dubonos, S.V.; Grigorieva, I.V.; Firsov, A.A. Electric field effect in atomically thin carbon films. *Science* **2004**, *306*, 666–669. [[CrossRef](#)]
2. Ci, L.; Song, L.; Jin, C.; Jariwala, D.; Wu, D.; Li, Y.; Srivastava, A.; Wang, Z.F.; Storr, K.; Balicas, L.; et al. Atomic Layers of Hybridized Boron Nitride and Graphene Domains. *Nat. Mater.* **2010**, *9*, 430. [[CrossRef](#)]
3. Wang, Q.H.; Kalantarzadeh, K.; Kis, A.; Coleman, J.N.; Strano, M.S. Electronics and optoelectronics of two-dimensional transition metal dichalcogenides. *Nat. Nanotechnol.* **2017**, *7*, 699–712. [[CrossRef](#)]
4. Hu, Z.Y.; Ding, Y.C.; Hu, X.M.; Zhou, W.H.; Yu, X.C.; Zhang, S.L. Recent progress in 2D group IV-IV monochalcogenides: synthesis, properties and applications. *Nanotechnology* **2019**, *30*, 252001. [[CrossRef](#)]
5. Xu, K.; Yin, L.; Huang, Y.; Shifa, T.A.; Chu, J.W.; Wang, F.; Cheng, R.Q.; Wang, Z.X.; He, J. Synthesis, properties and applications of 2D layered $\text{M}^{\text{III}}\text{X}^{\text{VI}}$ ($\text{M} = \text{Ga, In}$; $\text{X} = \text{S, Se, Te}$) materials. *Nanoscale* **2016**, *8*, 16802–16818. [[CrossRef](#)]
6. Yu, T.; Zhao, Z.Y.; Sun, Y.H.; Bergara, A.; Lin, J.Y.; Zhang, S.T.; Xu, H.Y.; Zhang, L.J.; Yang, G.C.; Liu, Y.C. Two-dimensional PC_6 with direct band gap and anisotropic carrier mobility. *J. Am. Chem. Soc.* **2019**, *141*, 1599–1605. [[CrossRef](#)]
7. Niedzielski, B.; Jia, C.; Berakdar, J. Supercurrent Induced by Chiral Coupling in Multiferroic/Superconductor Nanostructures. *Nanomaterials* **2021**, *11*, 184. [[CrossRef](#)] [[PubMed](#)]
8. Chittari, B.L.; Lee, D.; Banerjee, N.; MacDonald, A.H.; Hwang, E.; Jung, J. Carrier- and strain-tunable intrinsic magnetism in two-dimensional MAX_3 transition metal chalcogenides. *Phys. Rev. B* **2020**, *101*, 085415. [[CrossRef](#)]
9. Hou, W.; Mi, H.; Peng, R.; Peng, S.; Zeng, W.; Zhou, Q. First-Principle Insight into Ga-Doped MoS_2 for Sensing SO_2 , SOF_2 and SO_2F_2 . *Nanomaterials* **2021**, *11*, 314. [[CrossRef](#)] [[PubMed](#)]
10. Chen, J.; Xi, J.; Wang, D.; Shuai, Z. Carrier Mobility in Graphyne Should Be Even Larger than That in Graphene: A Theoretical Prediction. *J. Phys. Chem. Lett.* **2013**, *4*, 1443. [[CrossRef](#)] [[PubMed](#)]

11. Lherbier, A.; Botello-Mendez, A.R.; Charlier, J.C. Electronic and Transport Properties of Unbalanced Sublattice N-Doping in Graphene. *Nano Lett.* **2013**, *13*, 1446. [[CrossRef](#)] [[PubMed](#)]
12. Mak, K.F.; Lee, C.; Hone, J.; Shan, J.; Heinz, T.F. Atomically Thin MoS₂: A New Direct-Gap Semiconductor. *Phys. Rev. Lett.* **2010**, *105*, 136805. [[CrossRef](#)] [[PubMed](#)]
13. Ahmadi, M.; Zabihi, O.; Jeon, S.; Yoonessi, M.; Dasari, A.; Ramakrishna, S.; Naebe, M. 2D transition metal dichalcogenide nanomaterials: Advances, opportunities, and challenges in multi-functional polymer nanocomposites. *J. Mater. Chem. A* **2020**, *8*, 845–883. [[CrossRef](#)]
14. Cai, Y.Q.; Zhang, G.; Zhang, Y.W. Polarity-Reversed Robust Carrier Mobility in Monolayer MoS₂ Nanoribbons. *J. Am. Chem. Soc.* **2014**, *136*, 6269–6275. [[CrossRef](#)] [[PubMed](#)]
15. Anasori, B.; Lukatskaya, M.R.; Gogotsi, Y. 2D metal carbides and nitrides (MXenes) for energy storage. *Nat. Rev. Mater.* **2017**, *2*, 16098. [[CrossRef](#)]
16. Naguib, M.; Mochalin, V.N.; Barsoum, M.W.; Gogotsi, Y. 25th anniversary article: MXenes: A new family of two-dimensional materials. *Adv. Mater.* **2014**, *26*, 992–1005. [[CrossRef](#)]
17. Huang, K.; Li, Z.; Lin, J.; Han, G.; Huang, P. Two-dimensional transition metal carbides and nitrides (MXenes) for biomedical applications. *Chem. Soc. Rev.* **2018**, *47*, 5109–5124. [[CrossRef](#)]
18. Hong, Y.L.; Liu, Z.; Wang, L.; Zhou, T.; Ma, W.; Xu, C.; Feng, S.; Chen, L.; Chen, M.L.; Sun, D.M.; et al. Chemical vapor deposition of layered two-dimensional MoSi₂N₄ materials. *Science* **2020**, *369*, 670–674. [[CrossRef](#)]
19. Mortazavi, B.; Javvaji, B.; Shojaei, F.; Rabczuk, T.; Shapeev, A.V.; Zhuang, X.Y. Exceptional piezoelectricity, high thermal conductivity and stiffness and promising photocatalysis in two-dimensional MoSi₂N₄ family confirmed by first-principles. *Nano Energy* **2021**, *82*, 105716. [[CrossRef](#)]
20. Guo, S.D.; Zhu, Y.T.; Mu, W.Q.; Wang, L.; Chen, X.Q. Structure effect on intrinsic piezoelectricity in septuple-atomic-layer MoSi₂N₄ (M = Mo and W). *Comput. Mater. Sci.* **2021**, *188*, 110223. [[CrossRef](#)]
21. Guo, S.D.; Mu, W.Q.; Zhu, Y.T.; Wang, L.; Chen, X.Q.; Shapeev, A.V.; Zhuang, X.Y. Coexistence of intrinsic piezoelectricity and ferromagnetism induced by small biaxial strain in septuple-atomic-layer VSi₂P₄. *Phys. Chem. Chem. Phys.* **2020**, *22*, 28359–28364. [[CrossRef](#)] [[PubMed](#)]
22. Cao, L.M.; Zhou, G.H.; Wang, Q.Q.; Ang, L.K.; Ang, Y.S. Two-dimensional van der Waals electrical contact to monolayer MoSi₂N₄. *Appl. Phys. Lett.* **2021**, *118*, 013106. [[CrossRef](#)]
23. Ai, H.Q.; Liu, D.; Geng, J.Z.; Wang, S.P.; Lo, K.H.; Pan, H. Theoretical evidence of the spin-valley coupling and valley polarization in two-dimensional MoSi₂X₄ (X = N, P, and As). *Phys. Chem. Chem. Phys.* **2021**, *23*, 3144–3151. [[CrossRef](#)]
24. Mortazavi, B.; Javvaji, B.; Shojaei, F.; Rabczuk, T.; Shapeev, A.V.; Zhuang, X.Y. Valley pseudospin in monolayer MoSi₂N₄ and MoSi₂As₄. *Phys. Rev. B* **2021**, *103*, 035308.
25. Blöchl, P.E. Projector augmented-wave method. *Phys. Rev. B* **1994**, *50*, 17953. [[CrossRef](#)] [[PubMed](#)]
26. Kresse, G.; Furthmüller, J. Efficient iterative schemes for ab initio total-energy calculations using a plane-wave basis set. *Phys. Rev. B* **1996**, *54*, 11169. [[CrossRef](#)] [[PubMed](#)]
27. Perdew, J.P.; Burke, K.; Ernzerhof, M. Generalized Gradient Approximation Made Simple. *Phys. Rev. Lett.* **1996**, *77*, 3865–3868. [[CrossRef](#)]
28. Heyd, J.; Scuseria, G.E.; Ernzerhof, M. Hybrid Functionals Based on a Screened Coulomb Potential. *J. Chem. Phys.* **2003**, *118*, 8207–8215. [[CrossRef](#)]
29. Grimme, S.; Antony, J.; Ehrlich, S.; Krieg, H.A. consistent and accurate ab initio parametrization of density functional dispersion correction (DFT-D) for the 94 elements H–Pu. *J. Chem. Phys.* **2010**, *132*, 154104. [[CrossRef](#)]
30. Togo, A.; Tanaka, I. First Principles Phonon Calculations in Materials Science. *Scr. Mater.* **2015**, *108*, 1–5. [[CrossRef](#)]
31. Barnett, R.; Landman, U. Born-Oppenheimer Molecular-Dynamics Simulations of Finite Systems: Structure and Dynamics of (H₂O)₂. *Phys. Rev. B Condens. Matter Mater. Phys.* **1993**, *48*, 2081–2097. [[CrossRef](#)] [[PubMed](#)]
32. Taylor, J.; Guo, H.; Wang, J. Ab Initio Modeling of Quantum Transport Properties of Molecular Electronic Devices. *Phys. Rev. B Condens. Matter Mater. Phys.* **2001**, *63*, 245407. [[CrossRef](#)]
33. Guan, J.; Zhu, Z.; Tománek, D. Phase Coexistence and Metal-Insulator Transition in Few-Layer Phosphorene: A Computational Study. *Phys. Rev. Lett.* **2014**, *113*, 46804. [[CrossRef](#)] [[PubMed](#)]
34. Chen, P.J.; Jeng, H.T. High Applicability of Two-dimensional Phosphorous in Kagome Lattice Predicted from First-principles Calculations. *Sci. Rep.* **2016**, *6*, 23151.
35. Ahmad, S.; Mukherjee, S. A Comparative Study of Electronic Properties of Bulk MoS₂ and Its Monolayer using DFT Technique: Application of Mechanical Strain on MoS₂ Monolayer. *Graphene* **2014**, *3*, 52–59. [[CrossRef](#)]
36. Lee, C.; Wei, X.; Kysar, J.W.; Hone, J. Measurement of the elastic properties and intrinsic strength of monolayer graphene. *Science*, **2008**, *321*, 385–388. [[CrossRef](#)]
37. Michel, K.H.; Verberck, B. Theory of Elastic and Piezoelectric Effects in Two-dimensional Hexagonal Boron Nitride. *Phys. Rev. B Condens. Matter Mater. Phys.* **2009**, *80*, 224301. [[CrossRef](#)]
38. Andrew, R.C.; Mapasha, R.E.; Ukpong, A.M.; Chetty, N. Mechanical properties of graphene and boronitrene. *Phys. Rev. B Condens. Matter Mater. Phys.* **2012**, *85*, 125428 [[CrossRef](#)]
39. Yao, H.; Wang, Q.; Li, J.W.; Cai, W.S.; Wei, Y.D.; Wang, B.; Wang, J. Two-dimensional few-layer PC₃ as promising photocatalysts for overall water splitting. *Phys. Chem. Chem. Phys.* **2020**, *22*, 1485–1492. [[CrossRef](#)]

40. Wang, Q.; Li, J.W.; Liang, Y.; Nie, Y.N.; Wang, B. KAgSe: A New Two-Dimensional Efficient Photovoltaic Material with Layer-Independent Behaviors. *ACS Appl. Mater. Interfaces* **2018**, *10*, 41670–41677. [[CrossRef](#)]
41. Xie, J.; Zhang, Z.Y.; Yang, D.Z.; Xue, D.S.; Si, M.S. Theoretical Prediction of Carrier Mobility in Few-Layer BC₂N. *J. Phys. Chem. Lett.* **2014**, *5*, 4073–4077. [[CrossRef](#)]
42. Qiao, J.; Kong, X.; Hu, Z.X.; Yang, F.; Ji, W. High-mobility transport anisotropy and linear dichroism in few-layer black phosphorus. *Nat. Commun.* **2014**, *5*, 4475. [[CrossRef](#)] [[PubMed](#)]
43. Cui, Y.; Peng, L.; Sun, L.P.; Qian, Q.; Huang, Y.C. Two-dimensional few-layer group-III metal monochalcogenides as effective photocatalysts for overall water splitting in the visible range. *J. Mater. Chem. A* **2018**, *6*, 22768–22777. [[CrossRef](#)]
44. Radisavljevic, B.; Radenovic, A.; Brivio, J.; Giacometti, V.; Kis, A. Single-layer MoS₂ Transistors. *Nat. Nanotechnol.* **2011**, *6*, 147–150. [[CrossRef](#)] [[PubMed](#)]
45. Tan, W.C.; Huang, L.; Ng, R.J.; Wang, L.; Hasan, D.N.; Duffin, T.J.; Kumar, K.S.; Nijhuis, C.A.; Lee, C.; Ang, K.W. A Black Phosphorus Carbide Infrared Phototransistor. *Adv. Mater.* **2018**, *30*, 1705039. [[CrossRef](#)] [[PubMed](#)]
46. Long, M.; Gao, A.; Wang, P.; Xia, H.; Ott, C.; Pan, C.; Fu, Y.; Liu, E.; Chen, X.; Lu, W.; et al. Room Temperature High-Detectivity Mid-Infrared Photodetectors Based on Black Arsenic Phosphorus. *Sci. Adv.* **2017**, *3*, 700589. [[CrossRef](#)] [[PubMed](#)]
47. Kuzmenko, A.B. Kramers-Kronig. Constrained Variational Analysis of Optical Spectra. *Rev. Sci. Instrum.* **2005**, *76*, 083108. [[CrossRef](#)]
48. Gajdoš, M.; Hummer, K.; Kresse, G.; Furthmüller, J.; Bechstedt, F. Linear Optical Properties in the Projector-Augmented Wave Methodology. *Phys. Rev. B Condens. Matter Mater. Phys.* **2006**, *73*, 045112.
49. Zhang, L.; Gong, K.; Chen, J.; Liu, L.; Zhu, Y.; Xiao, D.; Guo, H. Generation and Transport of Valley-polarized Current in Transition-metal Dichalcogenides. *Phys. Rev. B Condens. Matter Mater. Phys.* **2014**, *90*, 195428. [[CrossRef](#)]
50. Xie, Y.; Zhang, L.; Zhu, Y.; Liu, L.; Guo, H. Photogalvanic Effect in Monolayer Black Phosphorus. *Nanotechnology* **2015**, *26*, 455202. [[CrossRef](#)]
51. Henrickson, L.E. Nonequilibrium Photocurrent Modeling in Resonant Tunneling Photodetectors. *J. Appl. Phys.* **2002**, *91*, 6273–6281. [[CrossRef](#)]
52. Pospischil, A.; Furchi, M.M.; Mueller, T. Solar-energy conversion and light emission in an atomic monolayer p-n diode. *Nat. Nanotechnol.* **2014**, *9*, 257–261. [[CrossRef](#)] [[PubMed](#)]
53. Zhao, P.; Yang, H.; Li, J.; Jin, H.; Wei, W.; Yu, L.; Huang, B.; Dai, Y. Design of New Photovoltaic Systems Based on Two-dimensional Group-IV Monochalcogenides for High Performance Solar Cells. *J. Mater. Chem. A* **2017**, *5*, 24145–24152. [[CrossRef](#)]